

FLOW OVER BLUFF BODIES WITH DIFFERENT SPANWISE WIDTHS IN A DEEP TURBULENT BOUNDARY LAYER

Xingjun Fang

Department of Mechanical Engineering
University of Manitoba
Winnipeg, MB, R3T 5V6, Canada
fangx@myumanitoba.ca

Mark F. Tachie

Department of Mechanical Engineering
University of Manitoba
Winnipeg, MB, R3T 5V6, Canada
mark.tachie@umanitoba.ca

ABSTRACT

This paper presents an investigation of the effects of different spanwise widths (S) on the spatio-temporal characteristics of turbulent flows over bluff bodies submerged in a deep turbulent boundary layer using a time-resolved particle image velocimetry. The Reynolds number based on free-stream velocity (U_∞) and bluff body height (H) is 12 300. The thickness of the oncoming turbulent boundary layer is $4.8H$. In total, 11 spanwise aspect ratios ($AR = S/H$) ranging from 1 to 20 were tested to study the transition process of flows over three-dimensional (3D) to nominally two-dimensional (2D) bluff bodies. The results exhibit three distinct regimes in terms of the variation of separation bubbles over and behind the bluff bodies with AR , namely, 2D regime, 3D regime and transitional regime. The reattachment length varies linearly with AR in the 3D regime, but remains constant in the 2D regime. Reynolds stresses over the bluff bodies increase monotonically as AR increases, however Reynolds stresses behind the bluff body with $AR = 8$ are stronger than the other cases. The low-frequency flapping motion of the separation bubble over the bluff bodies with $AR \geq 8$ is dominated by the oncoming streamwise elongated large-scale structures, whereas the flapping motion over the bluff body with $AR = 1$ is more related to the inherent vortex shedding motion. The interaction between the separation bubbles over and behind the bluff bodies is also strongly affected by AR .

INTRODUCTION

Separating and reattaching turbulent flows over surface-mounted bluff bodies are commonly encountered in environmental and industrial applications, such as atmospheric boundary layer over a cliff, building or vehicle. For these particular examples, the body height is typically much smaller than the thickness of the oncoming atmospheric boundary layer. As such, the flow that the bluff bodies see feature strong mean shear, high turbulent intensity and large-scale streamwise-elongated coherent structures. This can significantly alter the topology and dynamics of the sep-

aration bubbles, pressure fluctuations and vortical structures over and behind the bluff bodies. Although many existing research works were dedicated to the investigation of turbulent flows over either two-dimensional (2D) or three-dimensional (3D) bluff bodies, the flow characteristics over bluff bodies with an intermediate spanwise aspect ratio is still poorly understood. Therefore, this study aims at a systematic investigation of the effect of different spanwise aspect ratios on the spatio-temporal characteristics of turbulent flows over surface-mounted bluff bodies submerged in a deep turbulent boundary layer (TBL).

Flow over two-dimensional bluff bodies, such as forward-facing step (FFS), backward-facing step (BFS) and blunt plate, are popular canonical cases that are traditionally used to study geometry-induced flow separation and reattachment. Kiya & Sasaki (1983) observed different-sized vortex shedding events at different frequencies, and attributed the large-scale (low-frequency) unsteadiness to the enlargement/shrinkage of separation bubble induced by the flapping motion of shear layer. The periodic enlargement and shrinkage of separation bubbles, which is commonly termed as ‘flapping motion’, has also been observed in separation bubbles generated by FFS (Pearson *et al.*, 2013), BFS (Eaton & Johnston, 1982), blunt plate (Kiya & Sasaki, 1983) and 2D step (Fang & Tachie, 2019).

Flow around surface-mounted three-dimensional bluff bodies, such as cubes and square cylinders, with upstream laminar or thin turbulent boundary layer has also been extensively studied in the literature. For example, Hunt *et al.* (1978) theoretically and experimentally investigated the topology of flow around surface-mounted 3D bluff bodies. They showed that the number of nodes and saddles on walls satisfied case-dependent functions, reflecting the global three-dimensionality of flow around 3D bluff bodies. Hearst *et al.* (2016) studied the influence of oncoming free-stream turbulence on the wake flow behind a surface-mounted cube using particle image velocimetry and hot-wire anemometry. They concluded that high levels of oncoming turbulence enhance wake recovery and reduce the strength of vortex shedding.

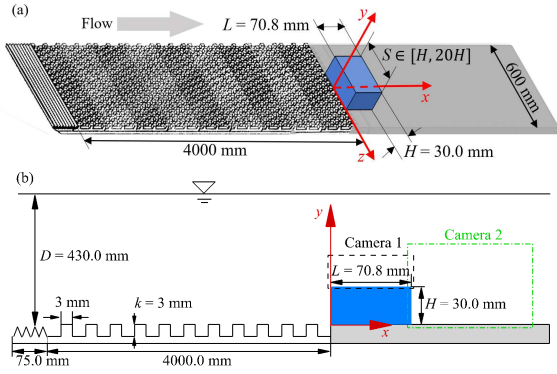


Figure 1. Schematic of experimental set-up and coordinate system (not to scale) in the (a) bird's eye view and (b) side view. The bluff body is indicated using a blue cuboid.

In spite of the extensive studies of flow over 2D and 3D bluff bodies, the transition process from fully 3D to nominally 2D flow as the AR of bluff bodies increases is still not well understood. This research topic, to our best knowledge, was only addressed by Martinuzzi & Tropea (1993) in the existing literature. In a fully-developed turbulent channel flow, Martinuzzi & Tropea (1993) measured mean flows around surface-mounted bluff bodies of the half channel height with different spanwise widths. The aim of the current research is to systematically investigate the effects of spanwise aspect ratio on turbulence statistics and spatio-temporal characteristics of coherent structures.

EXPERIMENTAL SET-UP AND TEST CASE

Experiments were conducted in a recirculating water channel located in the Turbulence and Hydraulic Engineering Laboratory (THEL) at the University of Manitoba. The test section of the water channel is of dimension 6000 mm \times 600 mm \times 450 mm (length \times width \times depth). Figure 1 shows schematic of the tested bluff bodies and coordinate system used in this paper. The streamwise, vertical and spanwise coordinates are denoted by x , y and z , respectively. To generate a deep TBL, 2D toothed barriers (75.0 mm long) followed by periodically repeated staggered cubic roughness elements (4000.0 mm long) is mounted on the bottom wall upstream the bluff bodies. The cross section in the x - y plane of the bluff bodies is fixed to 30.0 mm \times 70.8 mm ($L \times H$). Different spanwise widths (S) of the bluff bodies were tested to investigate the effect of a wide range of AR (S/H), including AR = 1, 2, 3, 3.5, 4, 5, 6, 8, 10, 12 and 20. Note that, in the case of AR = 20, the bluff body spans the entire width (600 mm) of the water channel. The Reynolds number based on the free-stream velocity ($U_\infty = 0.41$ m/s) and H is fixed to 12 300 for all the test cases.

The water was seeded by 10 μ m silver coated hollow glass particles, which have a specific gravity of 1.4. A diode pumped dual-cavity dual-head high speed Nd:YLF laser is used to illuminate the flow field. Each cavity of the laser generates a maximal pulse energy of 30 mJ/pulse at an operating frequency of 1000 Hz. The Davis 8.4 software provided by LaVision Inc. is used to control the data acquisition and velocity vector calculation. The raw images of illuminated particles are taken by high speed 12-bit CMOS cameras of a full resolution of 2560 pixel \times 1600 pixel.

To quantify the TBL upstream the bluff bodies, two

measurements were performed in the central x - y plane of the water channel without installing the bluff bodies. Specifically, the first measured used a large ($y/H \in [-0.3, 7.0]$) field of view (FOV) at a frequency of 1000 Hz, and the second measurement used a smaller ($y/H \in [-0.1, 3.2]$) FOV in the double-frame mode to achieve a better spatial resolution.

The measurements were conducted in x - y plane at the channel mid-span, with two cameras simultaneously capturing flows over and behind the step at a sampling frequency of 1000 Hz with a reduced resolution of 1920 pixel \times 1600 pixel. Specifically, considering the much stronger shear layer near the leading edge of the bluff bodies, a smaller FOV of 79.2 mm \times 64.8 mm is used over the bluff bodies using a Sigma 105 mm macro lens, whereas a Nikon 60 mm lens is used to capture a FOV of 197.1 mm \times 162.9 mm in the wake region. 32 000 samples were acquired for the bluff bodies with AR = 1.0, 3.5, 8.0 and 20.0, whereas 8000 samples were collected for the bluff bodies with AR = 2.0, 3.0, 4.0, 5.0, 6.0, 10.0 and 12.0.

The velocity vectors are computed using a multi-pass cross-correlation approach, and the final interrogation area (IA) is 32 pixel \times 32 pixel with 75% overlap. In this paper, the instantaneous velocity components along the streamwise (x) and vertical (y) directions are denoted by u and v , respectively. The operator (\cdot) represents temporal averaging. The mean velocities are also represented using an upper case for convenience, e.g., $\bar{u} \equiv U$. The fluctuating components are denoted by a superscript $(\cdot)'$, e.g., $u' \equiv u - U$. To concisely express each case, a notation of AR1 is used to denote the case of AR = 1, and so on for all other cases.

RESULTS AND DISCUSSION

Figure 2 characterizes the oncoming TBL of the bluff bodies by showing the profiles of streamwise mean velocity (U), the root-mean-square (RMS) of streamwise fluctuating velocity (u'_{rms}), as well as the premultiplied frequency spectra. The boundary layer thickness, $\delta = 4.8H$, is much higher than the body height. As such, the streamwise mean velocity at the body height ($U_H = 0.29$ m/s) is a more appropriate velocity scale for the following data representation (Lim *et al.*, 2007). The dimensionless mean shear at the body height ($T_H = \partial U / \partial y H / U_H$) is 0.23. The friction velocity (U_τ) is estimated to be 0.025 m/s and consequently, the wall coordinate of body height ($H^+ = H U_\tau / \nu$, where ν is the kinematic viscosity) is 750 and within the log layer. From figure 2(a), the value of u'_{rms} at the body height is 15.8% of U_H . As seen in figure 2(b), the streamwise fluctuating velocity near the body height possess a dominant frequency of $St = 0.069$. Assuming that the convective velocity is approximately U_H near the body height, this dominant frequency is associated with streamwise elongated structures of characteristic length 3δ . This length is close to the typical length scale of 2-3 δ for the well-recognized large-scale motion in the outer layer of TBL at high Reynolds numbers (Adrian *et al.*, 2000).

Figure 3 shows the mean flow fields at the mid-span in the two extreme AR cases. Regardless of AR, there exist distinct mean separation bubbles over and behind the bluff bodies, which are hereinafter denoted by TSBA and TSBB, respectively, for conciseness. Both TSBA and TSBB in the AR1 case are evidently much smaller than those in the AR20 case. In the AR1 case, the vertical elevation of the vortical core of TSBB is around $y/H = 0.8$. This value

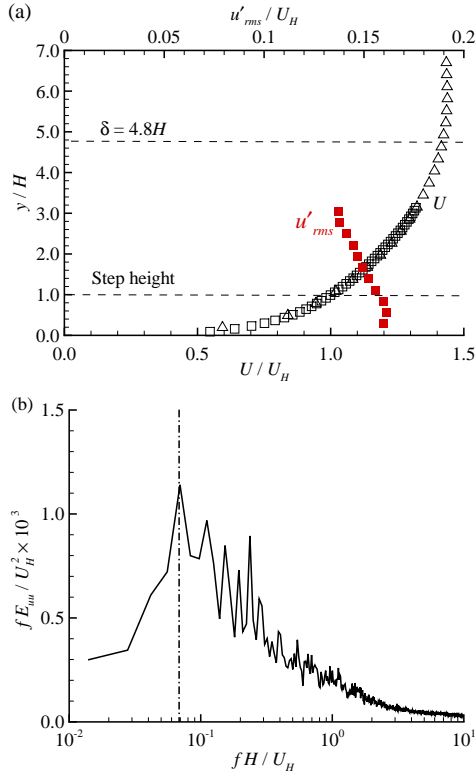


Figure 2. (a) Vertical profiles of U and u'_{rms} . (b) Premultiplied frequency spectra of streamwise fluctuating velocity at $y = H$ in the upstream location. The vertical line in (b) is at the frequency $St = fH/U_H = 0.069$.

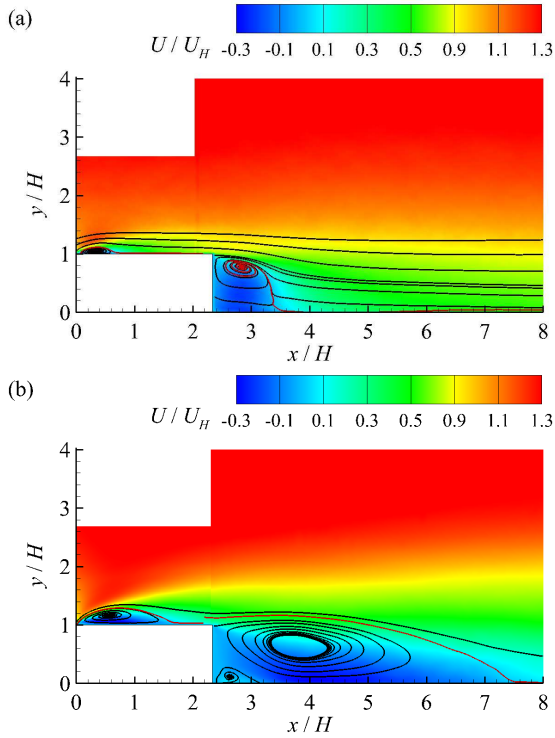


Figure 3. Contours of streamwise mean velocity (U) superimposed with mean streamlines in the (a) AR1 and (b) AR20 cases. The separating streamlines are plotted in red.

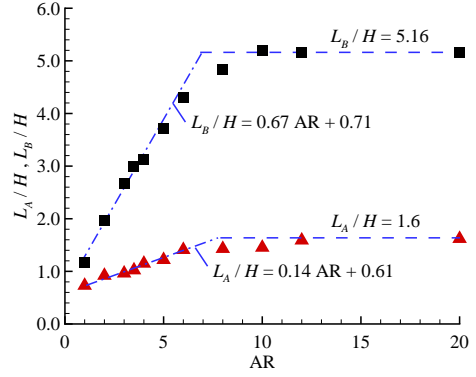


Figure 4. Variation of reattachment lengths over (L_A) and behind (L_B) the bluff bodies with AR . L_B is defined as the distance between the leeward face of the bluff body to the reattachment point. Linear equations are fitted for $AR \in [1, 6]$ using a least-squares-error method.

is very similar to those observed by Yakhot *et al.* (2006) and Hearst *et al.* (2016) in the wake of a surface-mounted cube.

Figure 4 plots the variation of reattachment lengths over (L_A) and behind (L_B) the bluff bodies with AR . Evidently, both L_A and L_B increase monotonically as AR increases, and remain constant for sufficiently large AR . The investigated range of AR can be categorized into three distinct regimes: (i) a 3D regime where L_A and L_B vary linearly with AR ; (ii) a 2D regime possessing asymptotic values of L_A and L_B ; and (iii) a transitional regime between the 3D and 2D regimes. The 3D regimes for L_A and L_B are both within the range $AR \in [1, 6]$, while the 2D regimes for L_A and L_B are for $AR \geq 12$ and $AR \geq 10$, respectively. These observations are in line with recommendation by Kiya & Sasaki (1983) and De Brederode & Bradshaw (1972) that bluff bodies of AR larger than 10 are necessary to produce nominally 2D flow at the mid-span. Based on the above results, we choose to focus more on the bluff bodies with $AR = 1, 8$ and 20 , so that all three different regimes are covered.

From figure 4, it is also evident that in the 3D regime, the slope $dL_B/dS = 0.67$ is much larger than the value of $dL_A/dS = 0.14$. This suggests that compared with TSBA, TSBB is more sensitive to the variation of AR . Moreover, the slope of fitted linear function by Martinuzzi & Tropea (1993) is identical to the present research (not shown here). On the contrary, the asymptotic values of L_B in Martinuzzi & Tropea (1993) are much larger than the present results. It is noted that the mean shear and turbulent intensity at the body height in the upstream location in Martinuzzi & Tropea (1993) are much weaker than the present study. Therefore, it is concluded that L_B in the 2D regime is sensitive to the oncoming flow condition, whereas L_B in the 3D regime is insensitive to the oncoming flow condition. Hearst *et al.* (2016) also observed that the reattachment length behind a surface-mounted cube is not affected by changes in the oncoming turbulence intensity or mean shear. Furthermore, L_A is strongly dependent on the oncoming flow condition in both 3D and 2D regimes. Nematollahi & Tachie (2018) observed that the reattachment length over an FFS decreased from $2.27H$ to $1.23H$ as the upstream relative turbulent intensity ($u'_{rms}|_{y=H}/U_H$) increased from 9.6% to 18.7% by enhancing the wall roughness.

Figure 5 shows representative vertical profiles of U

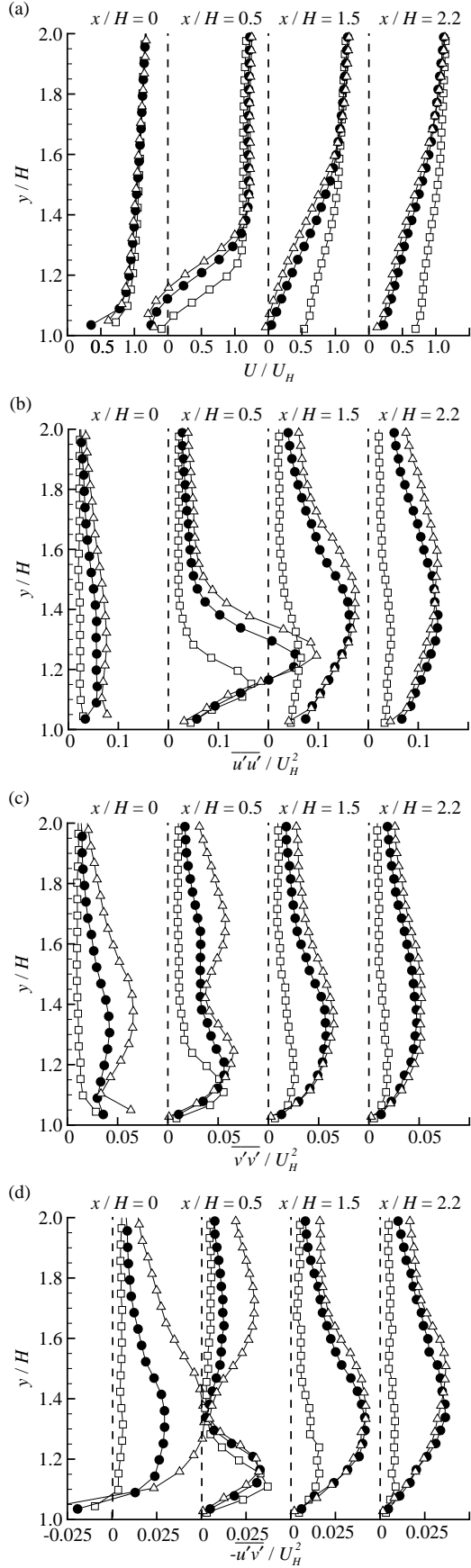


Figure 5. Vertical profiles of (a) U , (b) $\overline{u'u'}$, (c) $\overline{v'v'}$ and (d) $-\overline{u'v'}$ at selected streamwise locations over the bluff bodies with AR = 1 (hollow square), 8 (solid circle) and 20 (hollow triangle).

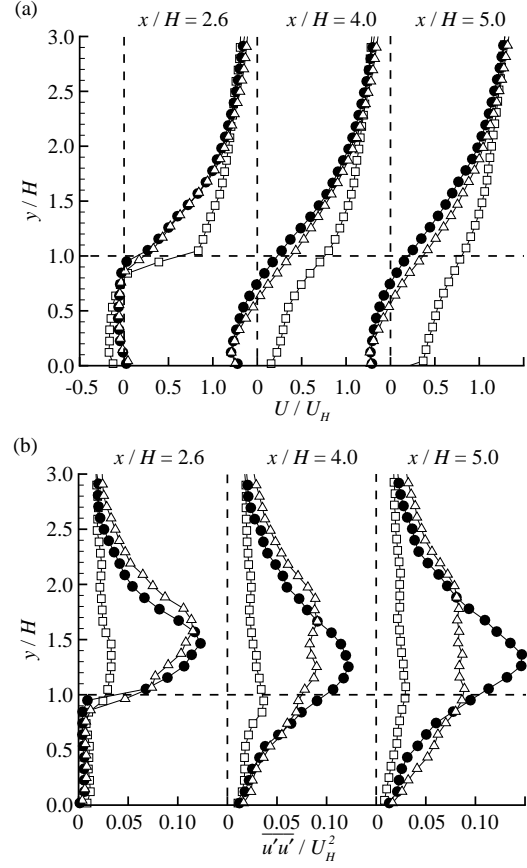


Figure 6. Vertical profiles of (a) U and (b) $\overline{u'u'}$ at selected streamwise locations behind the bluff bodies with AR = 1 (hollow square), 8 (solid circle) and 20 (hollow triangle).

and Reynolds stresses over the bluff bodies. In the region directly above the leading edge, the vertical profiles of U are almost identical regardless of AR, whereas the magnitudes of Reynolds stresses increase monotonically as AR increases. Negatively valued $-\overline{u'v'}$ appears in the immediate vicinity of the leading edge ($y/H < 1.1$), which is a hallmark of turbulent flows over bluff bodies (Fang & Tachie, 2019; Nematollahi & Tachie, 2018). At a streamwise location within the separation bubble (say $x/H = 0.5$), reverse flow occurs in the near-wall region and consequently, a shear layer is induced between the reverse flow area and far-stream region. This shear layer is away from the wall, and tends to roll up and generate spanwise vortices that are convected downstream (Lander *et al.*, 2016). At $x/H = 0.5$, the mean shear layer is mostly confined in the region below $y/H = 1.35$ and consequently there exist peak magnitudes of Reynolds stresses in this region. The profiles of $\overline{v'v'}$ and $-\overline{u'v'}$ in the AR20 case possess secondary local peaks above $y/H = 1.4$. This upper peak diminishes as AR decreases, and disappears in the AR1 case. Downstream of the center of separation bubbles over the bluff bodies (represented by $x/H = 1.5$ and 2.2), the reverse flow gradually disappears and the levels of Reynolds stresses decrease in the downstream direction. Near the top surface of the bluff bodies, the values of U in the AR8 and AR20 cases are smaller than the AR1 case.

Figure 6 plots the vertical profiles of U and $\overline{u'u'}$ in the wake region of the bluff bodies. Immediately downstream of the trailing edge of the bluff bodies (represented by $x/H = 2.6$), the profiles of U in the AR8 and AR20 cases

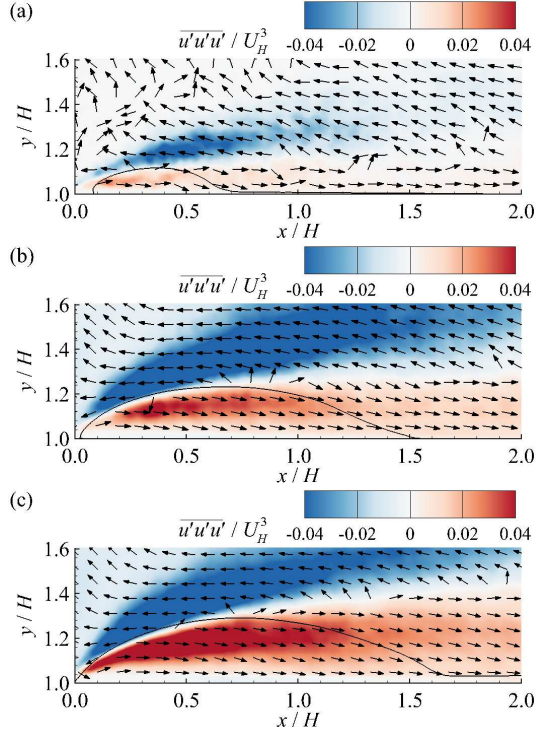


Figure 7. Contours of $\overline{u'u'u'}$ in the (a) AR1, (b) AR8 and (c) AR20 cases superimposed with the directional vectors ($u'u'u'$, $u'u'v'$). Also plotted are the separating streamlines.

are very close, whereas a steep change in U appears at the body height for $AR = 1$. This strong shear layer at $y = H$ downstream of the trailing edge for $AR = 1$ is attributed to the much larger near-wall U upstream of the trailing edge over the bluff bodies (see figure 5(a) for $x/H = 2.2$) compared to the other cases. In spite of the existence of the strongest shear layer at $x/H = 2.6$ in the AR1 case, the levels of $\overline{u'u'}$ for $AR = 1$ are still much weaker than those in the other cases. Indeed, the peak values of $\overline{u'u'}$ at $x/H = 2.6$ are close to those at $x/H = 2.2$ irrespective of AR. The shear layer developed behind the trailing edge of the bluff body with $AR = 1$ decays ($\partial U/\partial y$ decreases) quickly in the downstream direction, and the levels of the associated $\overline{u'u'}$ diminish as a consequence. In contrast, as x/H increases from 2.6 to 5.0, the peak values of $\overline{u'u'}$ in the AR8 case increase and even become larger than those in the AR20 case.

To investigate the turbulent transport of $\overline{u'u'}$ surrounding the separation bubble over the bluff bodies, figure 7 plots the third-order moments $\overline{u'u'u'}$ and $\overline{u'u'v'}$ over the bluff bodies with $AR = 1, 8$ and 20 . Regardless of AR, $\overline{u'u'u'}$ is negative immediately upstream the separation bubble, changes sign along the front half of the separating streamline and remains positive downstream of the separation bubble in the near-wall region, i.e., below the maximum height of separation bubble. From the directional vectors of ($u'u'u'$, $u'u'v'$) in figure 7, the turbulent transport of $u'u'$ is dominated by ejection events (featuring $u' < 0$ and $v' > 0$) immediately upstream of the separation, but by sweep events (featuring $u' > 0$ and $v' < 0$) within and downstream the separation bubble. This conclusion is also consistent with the observation by Elyasi & Ghaemi (2019) for a separation bubble induced by an adverse pressure gradient.

Figure 8 plots the premultiplied frequency spectra of reverse flow areas over and behind the bluff bodies, which

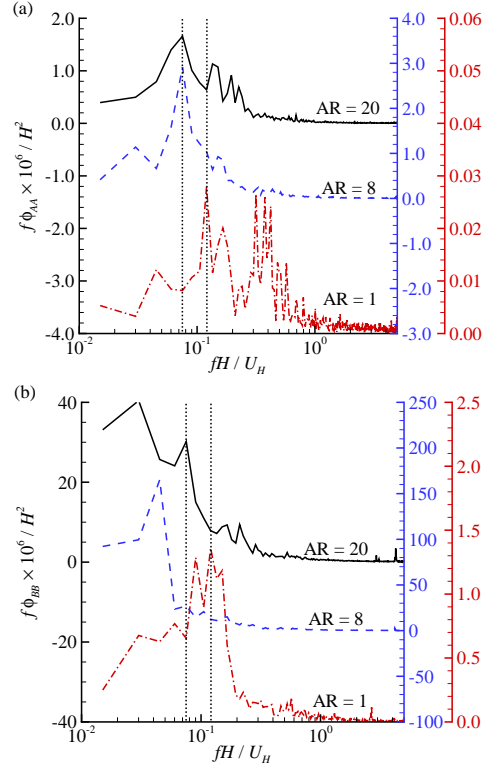


Figure 8. Premultiplied frequency spectra of (a) A_A ($f\phi_{AA}$) and (b) A_B ($f\phi_{BB}$). For clarity, each spectrum uses the vertical scale drawn with the same color. The dotted vertical lines mark frequencies at $St = 0.075$, and 0.12 , respectively.

are denoted by $f\phi_{AA}$ and $f\phi_{BB}$. The values of $f\phi_{AA}$ for $AR = 8$ and 20 both peak around $St = 0.075$. This frequency is close to the peak frequency of fE_{III} at the body height of the oncoming TBL (see figure 2(b)). On the other hand, the values of $f\phi_{BB}$ in the AR8 and AR20 cases peak at lower frequencies than $f\phi_{AA}$. These observations indicate that for $AR = 8$ and 20 , the separation bubble over the bluff bodies resonates with the oncoming TBL around $St = 0.075$, whereas the separation bubble behind the bluff bodies possesses much lower frequencies (equivalently, larger temporal scales). In contrast, both $f\phi_{AA}$ and $f\phi_{BB}$ for $AR = 1$ peak at $St = 0.12$. This frequency is close to the vortex shedding frequency observed by Hussein & Martinuzzi (1996) and Hearst *et al.* (2016) in the wake flow of a surface-mounted cube with oncoming TBL at lower mean shear and/or turbulent intensity. These observations indicate that flows over or behind the bluff body with $AR = 1$ is insensitive to the oncoming turbulence structure. It is also worth noting in figure 8(b) that the peak magnitude $f\phi_{BB}$ for $AR = 8$ is much larger than the other cases. This is consistent with the observation in figure 6(b) that the level of u'_{rms} below $y/H = 1.4$ is the strongest in the AR8 case.

To further investigate the interaction between TSBA and TSBB, figure 9 shows the temporal cross-correlation between A'_A and A'_B . It is straightforward that $R_{AB}(\Delta t > 0)$ reflects the influence of TSBA on TSBB, $R_{AB}(\Delta t < 0)$ evaluate the influence of TSBB on TSBA and $R_{AB}(\Delta t \approx 0)$ quantifies the synchronization between TSBA and TSBB. In the AR20 and AR1 cases, R_{AB} are very small for $\Delta t < 0$, and possess distinct peaks around $\Delta t U_H/H = 7.6$ and 5.0 , respectively. This indicates that in these two extreme cases,

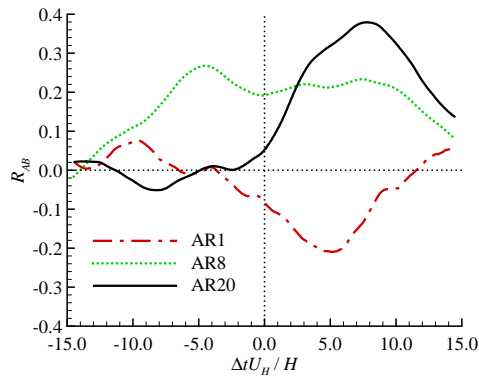


Figure 9. Temporal cross-correlation between A'_A and A'_B .

TSBA affects TSBB, but TSBB does not affect TSBA. Also, the peak magnitudes of R_{AB} in the AR20 and AR1 cases are positive and negative, respectively. This indicates that an enlarged TSBB ensues from an enlarged TSBA in the AR20 case, and conversely, an enlarged TSBB ensues from a shrunk TSBA in the AR1 case. Moreover, the values of R_{AB} in the AR8 case are significant over a wide range of $\Delta t^* \in [-5, 10]$. This indicates that TSBA and TSBB can mutually affect each other. Furthermore, the value of $R_{AB}(\Delta t = 0)$ is the largest in the AR8 case, indicating the best synchronization between TSBA and TSBB in this case.

CONCLUSIONS

Separating and reattaching flows over surface-mounted bluff bodies with different spanwise widths were studied using a time-resolved particle image velocimetry. In total, 11 different bluff bodies with spanwise aspect ratios ($AR = S/H$, where S and H represent the spanwise width and height of the bluff body, respectively) ranging from 1 to 20 were studied. The effects of different AR are studied in terms of the mean separation bubbles, Reynolds stresses as well as the unsteady characteristics of separation bubbles over and behind the bluff bodies.

The results show that there exists three distinct regimes based on the variation of separation bubbles over and behind the bluff bodies with AR, namely, 2D regime, 3D regime and transitional regime. The reattachment lengths over and behind the bluff bodies vary linearly with AR in the 3D regime at different rates. Over the bluff bodies, the reverse flow, shear layer and Reynolds stresses all increase monotonically as AR increases. Downstream of the trailing edge of the bluff body with $AR = 1$, very strong shear layer occurs but decays quickly in the downstream direction. In the wake region, the maximum level of $\overline{u'u'}$ for $AR = 8$ is stronger than those for the other cases. For $AR = 8$ and 20, the dominant frequencies of the separation bubbles over the bluff bodies coincide with the dominant frequency of the oncoming TBL, and the separation bubbles behind the bluff bodies possess apparently larger temporal scales. However, the separation bubbles over and behind the bluff body with $AR = 1$ possess an identical peak frequency, indicating its insensitivity to the turbulence structures embedded in the

oncoming TBL. The separation bubble over and behind the bluff body with $AR = 8$ can mutually affect each other, which is in sharp contrast to the cases of $AR = 1$ and 20.

ACKNOWLEDGEMENT

The financial support from Natural Sciences and Engineering Research Council (NSERC) of Canada and Canada Foundation for Innovation (CFI) to Mark F. Tachie is gratefully acknowledged.

REFERENCES

- Adrian, R. J., Meinhart, C. D. & Tomkins, C. D. 2000 Vortex organization in the outer region of the turbulent boundary layer. *J. Fluid Mech.* **422**, 1–54.
- De Brederode, V. & Bradshaw, P. 1972 Three-dimensional flow in nominally two-dimensional separation bubbles: I. Flow behind a rearward-facing step. *Tech. Rep.* pp. 72–19. Imperial College of Science and Technology.
- Eaton, J. K. & Johnston, J. P. 1982 Low frequency unsteadiness of a reattaching turbulent shear layer. *In Turbulent Shear Flows* **3**, 162–170.
- Elyasi, M. & Ghaemi, S. 2019 Experimental investigation of coherent structures of a three-dimensional separated turbulent boundary layer. *J. Fluid Mech.* **859**, 1–32.
- Fang, X. & Tachie, M. F. 2019 On the unsteady characteristics of turbulent separations over a forward-backward-facing step. *J. Fluid Mech.* **863**, 994–1030.
- Hearst, R. J., Gomit, G. & Ganapathisubramani, B. 2016 Effect of turbulence on the wake of a wall-mounted cube. *J. Fluid Mech.* **804**, 513–530.
- Hunt, J. C. R., Abell, C. J., Peterka, J. A. & Woo, H. 1978 Kinematical studies of the flows around free or surface-mounted obstacles; applying topology to flow visualization. *J. Fluid Mech.* **86**(1), 179–200.
- Hussein, H. J. & Martinuzzi, R. J. 1996 Energy balance for turbulent flow around a surface mounted cube placed in a channel. *Phys. Fluids* **8**(3), 764–780.
- Kiya, M. & Sasaki, K. 1983 Structure of a turbulent separation bubble. *J. Fluid Mech.* **137**, 83–113.
- Lander, D. C., Letchford, C. W., Amitay, M. & Kopp, G. A. 2016 Influence of the bluff body shear layers on the wake of a square prism in a turbulent flow. *Phys. Rev. Fluids* **1**, 044406.
- Lim, H. C., Castro, I. P. & Hoxey, R. P. 2007 Bluff bodies in deep turbulent boundary layers: Reynolds-number issues. *J. Fluid Mech.* **571**, 97–118.
- Martinuzzi, R. & Tropea, C. 1993 The flow around surface-mounted, prismatic obstacles placed in a fully developed channel flow. *ASME J. Fluids. Engng.* **115**, 85–92.
- Nematollahi, A. & Tachie, M. F. 2018 Time-resolved PIV measurement of influence of upstream roughness on separated and reattached turbulent flows over a forward-facing step. *AIP Adv.* **8**, 105110.
- Pearson, D. S., Goulart, P. J. & Ganapathisubramani, B. 2013 Turbulent separation upstream of a forward-facing step. *J. Fluid Mech.* **724**, 284–304.
- Yakhot, A., Liu, H. & Nikitin, N. 2006 Turbulent flow around a wall-mounted cube: a direct numerical simulation. *Int. J. Heat Fluid Flow* **27**, 994–1009.